

# A passively tunable mechanism for a dual bimorph energy harvester with variable tip stiffness and axial load

E Dehghan Niri and S Salamone<sup>1</sup>

Smart Structures Research Laboratory, Civil Structural and Environmental Engineering Department,  
State University of New York at Buffalo (UB), Buffalo, NY 14260, USA

E-mail: [ehsande@buffalo.edu](mailto:ehsande@buffalo.edu) and [ssalamon@buffalo.edu](mailto:ssalamon@buffalo.edu)

Received 28 September 2012, in final form 22 October 2012

Published 26 November 2012

Online at [stacks.iop.org/SMS/21/125025](http://stacks.iop.org/SMS/21/125025)

## Abstract

This paper presents a novel vibration-based piezoelectric energy harvester capable of passively tuning its resonant frequency to a wide range of frequencies. The device comprises a dual bimorph with a mass at its free end. A novel sliding mechanism, consisting of two oblique springs connected to the tip mass, is proposed to widen the resonance frequency of the device even to very low frequencies. The application of two oblique springs results in an additional stiffness and axial load that are introduced within the system, such that the resonance frequency of the device is now a function of both the stiffness and axial load associated with the spring forces. An operator can manually change the resonance frequency of the harvester just by small adjustments of the sliding mechanism. Further, the device allows one to tune the resonance frequency of the beam to match very low frequencies without the requirement of having a large proof mass. The analytical solution of an axially loaded cantilevered piezoelectric energy harvester with tip stiffness, using Euler–Bernoulli beam assumptions, is presented. A parametric case study is presented to demonstrate the performance of the device.

(Some figures may appear in colour only in the online journal)

## 1. Introduction

Vibration-based energy harvesting has become the focus of considerable research effort in the last decade. This increase in research has been brought on by modern advances in low-power-consumption devices and the need to provide wireless technology. Vibration energy can be converted to electrical energy through three main kinds of transduction mechanism: electrostatic, electromagnetic and piezoelectric. Among these transduction mechanisms, piezoelectric transduction has recently received the greatest attention mainly due to the large power density, ease of application and direct conversion of mechanical to electrical energy [1].

Cantilevered beams with one (i.e., unimorph) or two (i.e., bimorph) piezoceramic layers are the most popular

forms of piezoelectric energy harvesters. The main drawback of these devices is that to be efficient, their resonance frequency needs to match exactly the frequency of the ambient vibration [2–8]. Even small frequency mismatches between the harvester resonant frequency and the dominant frequency of excitation can cause significant decreases in power output.

Several approaches have been proposed to broaden the frequency range of these devices, such as devices with multiple cantilever beams with different lengths and tip masses [3]. It has been shown that multiple beams can efficiently operate in a wide band of frequencies; however, the geometry of this kind of device may negatively affect the cost and size of the harvester. A nonlinear mechanical resonator has been proposed in several studies to enlarge the energy harvester's power bandwidth [9–13]. In Cornwell *et al* [14] a tuned axillary structure was attached to the host structure to overcome the limitation of low power output at a low excitation frequency; however, this method requires

<sup>1</sup> Author to whom any correspondence should be addressed.

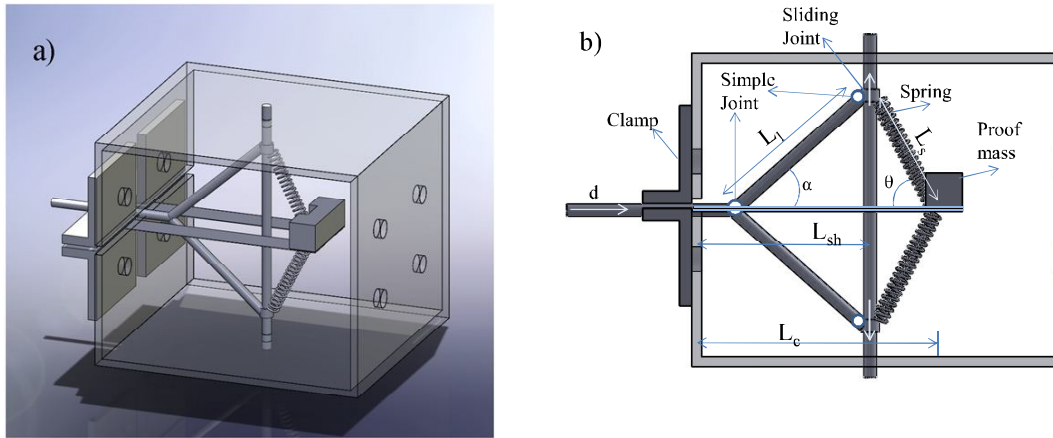


**Figure 1.** The proposed tunable energy harvester: (a) 3D view and (b) plan view .

a prior knowledge about the excitation frequency of the host structure. An active self-tuning device was proposed in [15]. The main limitation of an active approach is the requirement of additional power to change the dynamic or electronic properties of the harvester [16]. In contrast, a passive approach only requires an initial power to tune the device; as a result, interest in this topic has continually grown in the past few years. Wu *et al* [17] proposed a movable mass to change the frequency of the resonator. A self-tunable piezoelectric harvester of movable cantilever couples was investigated by Jo *et al* [18]. The proposed device was able to work in two phases in which four tuned frequencies could be achieved. Gu and Livermore [19, 20] exploited the centrifugal force of a rotational system to provide tensile stress and change the resonance frequency of a harvester for rotating applications. A novel simply supported bimorph with a variable compressive axial preload was proposed in [2] in order to reduce the stiffness of the beam and, as a consequence, the resonance frequency of the harvester. It has been shown that the compressive load can be used to tune the harvester and to improve the efficiency of the piezoceramic layers by increasing the electromechanical coupling coefficient [21]. An axial preload effect on the power generation and shift frequency of a piezoelectric cantilevered beam was numerically investigated by Hu *et al* [22]. Eichhorn *et al* [23] proposed a piezoelectric cantilevered beam with two additional arms that were used to provide compressive and tensile load to the tip of the beam in order to reduce and increase the frequency of the energy harvester. A magnetic force was used in [4] in order to change the tip stiffness and as a result the frequency tuning of a cantilever beam; however, the performance of this device in an environment with magnetic interference may be not reliable. A low-frequency zigzag piezoelectric energy harvester was proposed in [24] and validated by a comprehensive parametric study.

In this work a novel tunable vibration energy scavenger is proposed that provides mechanically variable and adjustable tip stiffness and axial load for a bimorph piezoelectric energy harvester. An analytical model is used to show the performance of the device.

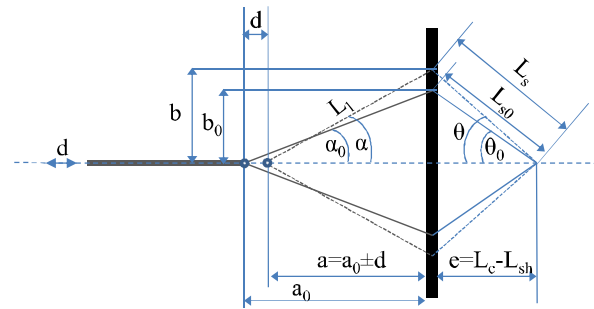


**Figure 2.** The schematic geometry of the device.

The paper begins by an overview of the proposed device. An analytical solution for the vibrating bimorph cantilever beam with tip stiffness and axial load is presented in section 3. This is followed by section 4, which reports the results of a case study, followed by the conclusion in section 5.

## 2. Overview of the proposed tunable energy harvester

The proposed device consists of two parallel bimorphs clamped at one end and connected to each other at the other end, as shown in figure 1. A sliding mechanism is used to change the equivalent vertical stiffness and the axial load applied by two springs attached to the tip of the dual beam. As a result, the dynamic behavior of the system can be tuned manually by an operator according to the dominant frequency of the intended environment.

A kinematic mechanism associated to a given displacement ( $d$ ) of the sliding part is shown in figure 2. Theoretically, two extreme positions can be defined, that is,  $\alpha = 0^\circ$  and  $90^\circ$ , which correspond to minimum and maximum stiffness, respectively. However, it is recommended to impose an initial position ( $\theta_0$  or  $\alpha_0$ ) for the mechanism so that it can be changed around this, to increase or decrease the resonance frequency of the energy harvester, as will be shown in section 4. Based

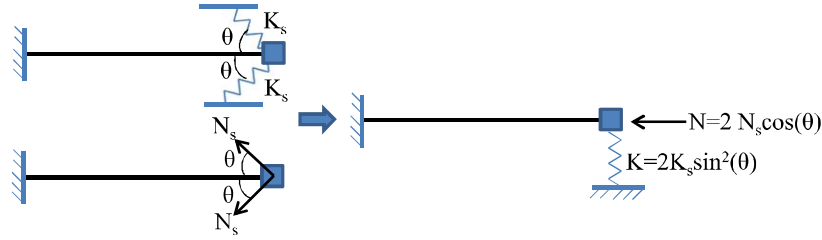


**Figure 3.** A schematic view of the device with its equivalent cantilever beam with mass, axial load and stiffness at the tip.

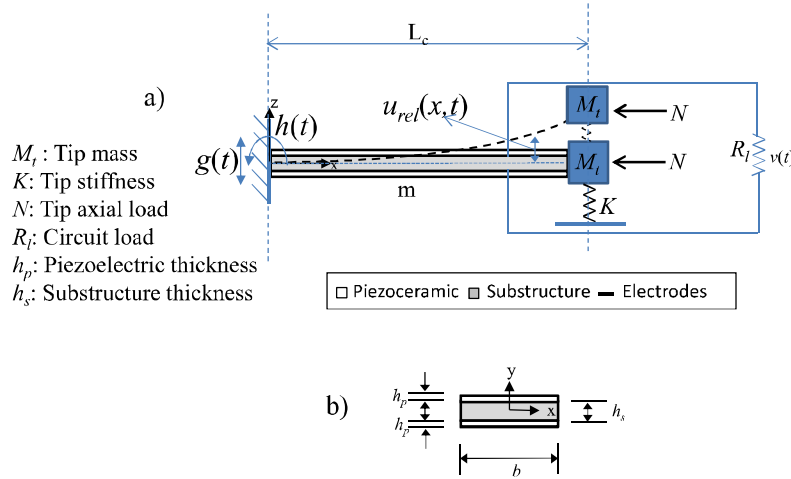


**Figure 4.** Configurations of a geometrically uniform bimorph piezoelectric energy harvester with tip axial load and stiffness and excited by translation and rotation of its base. (a) Circuit connection of the piezoceramic layers of bimorph with relative displacement and (b) their cross-sectional view.

on geometrical considerations and since  $L_1$  and  $e$  are fixed

$$\alpha = \arccos\left(\frac{a_0 \pm d}{L_1}\right) \quad (1)$$

$$\theta = \arctan\left(\frac{L_1 \sin(\alpha)}{e}\right) \quad (2)$$

where  $a_0$ ,  $d$ ,  $e$  and  $L_1$  are shown in figure 2.

To investigate the dynamic behavior of the proposed device the equivalent beam shown in figure 3 is considered. Under the assumption of small displacements, the vertical stiffness ( $K$ ) and axial load ( $N$ ) at the tip of the beam are proportional to  $\sin^2(\theta)$  and  $\cos(\theta)$ , respectively [25]; therefore, the following relationships can be defined:

$$K = 2K_s \sin^2(\theta) \quad (3a)$$

$$N = 2N_s \cos(\theta) \quad (3b)$$

where  $K_s$  is the stiffness of each spring,  $\theta$  is the spring angle to the  $x$  axis of the beam and  $N_s$  is the force exerted by each spring. It can be observed that the values of  $K$  and  $N$  can be modified by changing the angle  $\theta$ . The damping component as a result of the tip spring is not shown in figure 3; however, in section 3 it will be considered in the equation of motion.

In section 3 the equations governing the electromechanical behavior of the proposed device are presented.

### 3. An analytical model of a cantilevered bimorph with tip mass, stiffness and axial load

This section presents the modal analysis of the cantilevered bimorph shown in figure 4. To the best of the authors' knowledge, the dynamic response analysis of a piezoelectric cantilevered beam with tip stiffness and axial load has not been reported in any previous research.

By having the modal frequencies and shape functions in the same fashion as presented in [26], the voltage and power frequency response function of the system will be defined in a closed-form solution.

#### 3.1. Coupled mechanical equation and modal analysis

The cantilever beam shown in figure 4 is subjected to arbitrary translation and rotation motions of its base, which are denoted by  $g(t)$  and  $h(t)$  respectively. The effective transverse base displacement  $u_b(x, t)$  can be written as [26]

$$u_b(x, t) = g(t) + xh(t). \quad (4)$$

Using the Euler–Bernoulli beam theory, the partial differential equation for an axially loaded cantilever beam with tip mass under base excitation has been defined by Erturk *et al* [26]. On the addition of tip axial load the partial differential equation

is [27]

$$\begin{aligned} & -\frac{\partial^2 M(x, t)}{\partial x^2} + c_s I \frac{\partial^5 u_{\text{rel}}(x, t)}{\partial x^4 \partial t} \\ & + c_t \delta(x - L_c) \frac{\partial u_{\text{rel}}(x, t)}{\partial t} \\ & + m \frac{\partial^2 u_{\text{rel}}(x, t)}{\partial t^2} + N \frac{\partial^2 u_{\text{rel}}(x, t)}{\partial x^2} \\ & = -[m + M_t \delta(x - L_c)] \frac{\partial^2 u_b(x, t)}{\partial t^2} \end{aligned} \quad (5)$$

where  $M(x, t)$  is the internal bending moment,  $c_s$  is the equivalent damping coefficient of the composite cross section,  $c_t$  is the equivalent vertical damping coefficient of the springs at the tip of the beam,  $I$  is the equivalent area moment of inertia of the composite cross section,  $m$  is the mass per unit length of the beam,  $L_c$  is the length of beam and  $\delta(x)$  is the Dirac delta function. It should be noted that  $N$  is not tangential, that is, the direction of  $N$  is considered to be always horizontal.

In equation (5)  $m$  is defined as

$$m = b(\rho_s h_s + 2\rho_p h_p) \quad (6)$$

where  $b$  is the width,  $\rho_s$  is the mass density of the substructure material,  $\rho_p$  is the density of the piezoceramic material,  $h_s$  is the substructure thickness and  $h_p$  is the piezoelectric thickness, as shown in figure 4(b).

Instead of defining damping coefficients in the physical equation of motion, an undamped system is considered, by setting  $c_s I$  and  $c_t$  to zero in equation (5) [26]; therefore, the modal damping is used in the equation in modal coordinates, as is common in practice. It is noteworthy that it is common in many dynamic problems for the sake of simplicity to approximate the different damping components by an equivalent modal damping ratio. The internal bending moment  $M(x, t)$  is the integral of the first moment of the axial stress over the cross section [26]

$$\begin{aligned} M(x, t) = b & \left( \int_{-h_p - \frac{h_s}{2}}^{-\frac{h_s}{2}} T_1^p z \, dz + \int_{-\frac{h_s}{2}}^{\frac{h_s}{2}} T_1^s z \, dz \right. \\ & \left. + \int_{\frac{h_s}{2}}^{h_p + \frac{h_s}{2}} T_1^p z \, dz \right) \end{aligned} \quad (7)$$

where  $T_1^p$  and  $T_1^s$  are the axial stress in the piezoelectric and the main structure layer, respectively, which are given by the following constitutive relations:

$$T_1^s = Y_s S_1^s, \quad T_1^p = c_{11}^E S_1^p - e_{31} E_3 \quad (8)$$

where  $Y_s$  is the Young's modulus of the substructure layer,  $c_{11}^E$  is the Young's modulus of the piezoceramic layer at constant electric field,  $e_{31}$  is the piezoelectric constant and  $E_3$  is the electric field component, in the  $z$  direction. The subscript and superscript  $s$  and  $p$  stand for the substructure and piezoceramic layer respectively. Under the assumption of plane stress, the Young's modulus of the piezoceramic layer can be expressed as  $c_{11}^E = \frac{1}{S_{11}^E}$ , where  $S_{11}^E$  is the elastic compliance at constant electric field [28]. Also,  $e_{31}$  can be

defined in terms of the piezoelectric constant  $d_{31}$  as  $e_{31} = \frac{d_{31}}{S_{11}^E}$ . It should be noted that, since the electrodes covering the opposite transverse faces of the piezoelectric layers are very thin, as compared to the overall thickness of the harvester, their contribution to the thickness dimension is negligible. The axial strain components in the piezoelectric  $S_1^p$  and substructure  $S_1^s$  at location  $z$  from the neutral axis of the beam, based on Euler–Bernoulli beam theory, are proportional to the curvature as

$$S_1(x, z, t) = -z \frac{\partial^2 u_{\text{rel}}(x, t)}{\partial x^2}. \quad (9)$$

The length to thickness aspect ratio of the beam is usually high enough to neglect the shear effect; as a result the Euler–Bernoulli theory can be considered an appropriate assumption. Equations (8) and (9) are obtained under the assumption that the layers are perfectly bonded and exhibit linear elastic material behavior.

Considering that the piezoelectric layers of a bimorph can be combined in two configurations, that is, series or parallel, the electric field  $E_3$  in equation (8) should be expressed in terms of the respective voltage term (i.e.,  $v_s(t)$ ,  $v_p(t)$ ) for each configuration [29] using the following relationships:

$$E_3(t) = -\frac{v_s(t)}{2h_p} \quad \text{for series} \quad (10a)$$

$$E_3(t) = -\frac{v_p(t)}{h_p} \quad \text{for parallel.} \quad (10b)$$

The inertial bending moment can be obtained for a series or parallel circuit from equation (7) as [26]

$$M(x, t) = -YI \frac{\partial^2 u_{\text{rel}}(x, t)}{\partial x^2} + \Gamma v(t)[H(x) - H(x - L_c)] \quad (11)$$

where  $YI$  is the bending stiffness term of the composite cross section for a constant electric field,  $\Gamma$  is the coefficient of the backward coupling term and  $H(x)$  is the Heaviside step function.

Substituting equation (11) into (5) the coupled beam equation for the series configuration can be obtained as

$$\begin{aligned} & YI \frac{\partial^4 u_{\text{rel}}(x, t)}{\partial x^4} + c_s I \frac{\partial^5 u_{\text{rel}}(x, t)}{\partial x^4 \partial t} \\ & + c_t \delta(x - L_c) \frac{\partial u_{\text{rel}}(x, t)}{\partial t} \\ & + m \frac{\partial^2 u_{\text{rel}}(x, t)}{\partial t^2} + N \frac{\partial^2 u_{\text{rel}}(x, t)}{\partial x^2} \\ & - \Gamma v_s(t) \left[ \frac{d\delta(x)}{dx} - \frac{d\delta(x - L_c)}{dx} \right] \\ & = -[m + M_t \delta(x - L_c)] \frac{\partial^2 u_b(x, t)}{\partial t^2}. \end{aligned} \quad (12)$$

The coefficient of the backward coupling term for the series configuration in equation (12) is [26]

$$\Gamma = \frac{e_{31} b}{2h_p} \left[ \left( h_p + \frac{h_s}{2} \right)^2 - \frac{h_s^2}{4} \right]. \quad (13)$$

This coefficient for the parallel configuration is  $2\Gamma$ . The coupled beam equation for parallel configurations can be obtained from equation (12) by changing  $\Gamma$  to  $2\Gamma$ .

The equivalent bending stiffness term  $YI$  in equation (12) is [20]

$$YI = \frac{2b}{3} \left\{ Y_s \frac{h_s^3}{8} + c_{11}^E \left[ \left( h_p + \frac{h_s}{2} \right)^3 - \frac{h_s^3}{8} \right] \right\}. \quad (14)$$

To solve the differential equation (12) using the method of separation of variables [30], four boundary conditions are needed.

The boundary conditions at  $x = 0$  are

$$u_{\text{rel}}(0, t) = 0, \quad \left. \frac{\partial u_{\text{rel}}(x, t)}{\partial x} \right|_{x=0} = 0. \quad (15)$$

The boundary condition at  $x = L_c$  for the bending moment can be expressed as [20]

$$\left[ YI \frac{\partial^2 u_{\text{rel}}(x, t)}{\partial x^2} + I_t \frac{\partial^3 u_{\text{rel}}(x, t)}{\partial t^2 \partial x} \right]_{x=L_c} = 0 \quad (16)$$

where  $I_t$  is the mass moment of inertia of the proof mass; the shear boundary condition considering axial load is [31]

$$\left[ YI \frac{\partial^3 u_{\text{rel}}(x, t)}{\partial x^3} - M_t \frac{\partial^2 u_{\text{rel}}(x, t)}{\partial t^2} - K u_{\text{rel}}(x, t) + N \frac{\partial^2 u_{\text{rel}}(x, t)}{\partial x^2} \right]_{x=L_c} = 0 \quad (17)$$

where  $K$  and  $N$  are defined in (3). Equation (17) is where the effect of tip stiffness shows itself.

The method of separation of variables can be used to solve the differential equation defined in equation (12) as

$$u_{\text{rel}}(x, t) = \phi(x) \eta(t) \quad (18)$$

where  $\phi(x)$  is the modal eigenfunction and  $\eta(t)$  is the modal mechanical coordinate expression. It should be mentioned that  $\phi(x)$  is the same for both series and parallel configurations while  $\eta(t)$  is different. Based on the proportional damping assumption and substitution of equation (18) into equation (12) for free vibration leads to [27]

$$\frac{YI}{\phi(x)} \frac{d^4 \phi(x)}{dx^4} + \frac{N}{\phi(x)} \frac{d^2 \phi(x)}{dx^2} = -\frac{m}{\eta(t)} \frac{d^2 \eta(t)}{dt^2} = \gamma \quad (19)$$

where  $\gamma$  is a constant. Replacing  $\gamma$  by  $m\omega^2$  one can obtain two separated differential equations in the time and space domains as

$$\frac{d^2 \eta(t)}{dt^2} + \omega^2 \eta(t) = 0 \quad (20)$$

$$YI \frac{d^4 \phi(x)}{dx^4} + N \frac{d^2 \phi(x)}{dx^2} - m\omega^2 \phi(x) = 0. \quad (21)$$

Equation (21) leads to frequency and mode-shape expressions for the free vibration, in which the axial load  $N$  is a basic dynamic parameter. Dividing equation (21) by  $YI$  leads to

$$\frac{d^4 \phi(x)}{dx^4} + q^2 \frac{d^2 \phi(x)}{dx^2} - a^4 \phi(x) = 0 \quad (22)$$

where  $q$  and  $a$  are defined as

$$q^2 = \frac{N}{YI} \quad (23a)$$

$$a^4 = \frac{m\omega^2}{YI}. \quad (23b)$$

A general solution for equation (22) is [27]

$$\phi(x) = D_1 \sin(\beta x) + D_2 \cos(\beta x) + D_3 \sinh(\varepsilon x) + D_4 \cosh(\varepsilon x) \quad (24)$$

where  $\varepsilon$  and  $\beta$  can be obtained by solving the characteristic function of  $(s^4 + q^2 s^2 - a^4 = 0)$  for  $s$ ,

$$\varepsilon = \sqrt{\left( a^4 + \frac{q^4}{4} \right)^{\frac{1}{2}} - \frac{q^2}{2}} \quad (25a)$$

$$\beta = \sqrt{\left( a^4 + \frac{q^4}{4} \right)^{\frac{1}{2}} + \frac{q^2}{2}}. \quad (25b)$$

Considering the boundary conditions in equations (15)–(17), the modal frequencies (eigenvalues) and the coefficients  $D_1, D_2, D_3$ , and  $D_4$  can be obtained. Substitution of equation (24) into the geometric boundary conditions defined in equations (15)–(17), gives

$$\begin{bmatrix} 0 & 1 & 0 & 1 \\ \beta & 0 & \varepsilon & 0 \\ \Lambda_{31} & \Lambda_{32} & \Lambda_{33} & \Lambda_{34} \\ \Lambda_{41} & \Lambda_{42} & \Lambda_{43} & \Lambda_{44} \end{bmatrix} \begin{bmatrix} D_1 \\ D_2 \\ D_3 \\ D_4 \end{bmatrix} = 0. \quad (26)$$

In equation (26), the first two rows are derived from the boundary conditions defined in equation (15), whereas the  $\Lambda_{ij}$  are derived from the boundary conditions in equations (16) and (17) as follows:

$$\Lambda_{31} = -I_t \beta \omega^2 \cos(\beta L) - YI \beta^2 \sin(\beta L) \quad (27)$$

$$\Lambda_{32} = I_t \beta \omega^2 \sin(\beta L) - YI \beta^2 \cos(\beta L) \quad (28)$$

$$\Lambda_{33} = -I_t \varepsilon \omega^2 \cosh(\varepsilon L) + YI \varepsilon^2 \sinh(\varepsilon L) \quad (29)$$

$$\Lambda_{34} = -I_t \varepsilon \omega^2 \sinh(\varepsilon L) + YI \varepsilon^2 \cosh(\varepsilon L) \quad (30)$$

$$\Lambda_{41} = M_t \omega^2 \sin(\beta L) - YI \beta^3 \cos(\beta L) - K \sin(\beta L) - N \beta \cos(\beta L) \quad (31)$$

$$\Lambda_{42} = M_t \omega^2 \cos(\beta L) + YI \beta^3 \sin(\beta L) - K \cos(\beta L) + N \beta \sin(\beta L) \quad (32)$$

$$\Lambda_{43} = M_t \omega^2 \sinh(\varepsilon L) + YI \varepsilon^3 \cosh(\varepsilon L) - K \sinh(\varepsilon L) - N \varepsilon \cosh(\varepsilon L) \quad (33)$$

$$\Lambda_{44} = M_t \omega^2 \cosh(\varepsilon L) + YI \varepsilon^3 \sinh(\varepsilon L) - K \cosh(\varepsilon L) - N \varepsilon \sinh(\varepsilon L). \quad (34)$$

For nontrivial solutions to exist, the following determinant is required to vanish, and this defines the characteristic function



to find modal frequencies or eigenvalues

$$\begin{vmatrix} 0 & 1 & 0 & 1 \\ \beta & 0 & \varepsilon & 0 \\ \Lambda_{31} & \Lambda_{32} & \Lambda_{33} & \Lambda_{34} \\ \Lambda_{41} & \Lambda_{42} & \Lambda_{43} & \Lambda_{44} \end{vmatrix} = 0. \quad (35)$$

Solving equation (35) for  $\omega$ , infinite eigenvalues  $\omega_r$  are obtained.

By substituting each eigenvalue  $\omega_r$  in equations (23b) and (24), the mode shapes are obtained as

$$\begin{aligned} \phi_r(x) = A_r \left[ \sin(\beta_r x) - \frac{\beta_r}{\varepsilon_r} \sinh(\varepsilon_r x) \right. \\ \left. + \Gamma_r (\cos(\beta_r x) - \cosh(\varepsilon_r x)) \right] \end{aligned} \quad (36)$$

where  $\Gamma_r$  is

$$\Gamma_r = \frac{\frac{\beta_r}{\varepsilon_r} \Lambda_{33r} - \Lambda_{31r}}{\Lambda_{32r} - \Lambda_{34r}} \quad (37)$$

and  $A_r$  is a modal amplitude constant that can be evaluated using mass normalization based on orthogonality of the modal shape functions [29]

$$\begin{aligned} \int_0^{L_c} \phi_s(x) m \phi_r(x) dx + \phi_s(L_c) M_t \phi_r(L_c) \\ + \left[ \frac{d\phi_s(x)}{dx} I_t \frac{d\phi_r(x)}{dx} \right]_{x=L_c} = \delta_{sr} \end{aligned} \quad (38)$$

where  $\delta_{sr}$  is the Kronecker delta function. The normalized modal shape functions  $\phi_r(x)$  are the same for series and parallel configurations based on the zero load ( $R_l = 0$ ) assumption (short circuit). For non-zero values of the load resistance the modal coordinates  $\eta_r(t)$  are different since a point moment as a result of voltage appears in the coupled beam equation (12) [26].

The beam has infinite vibration modes, so the general response is a linear combination of all vibration modes

$$u_{rel}(x, t) = \sum_{r=1}^{\infty} \phi_r(x) \eta_r(t). \quad (39)$$

It is noteworthy that one can find the critical load  $N_{cr}$  by setting  $\omega = 0$  and solving equation (35) for  $N$ .

To evaluate the behavior of this device, the dimensionless tip stiffness and axial load are defined as  $\hat{K} = \frac{K}{\bar{K}}$  and  $\hat{N} = \frac{N}{\bar{N}}$  respectively, where  $\bar{K} = \frac{3YI}{L^3}$  is the theoretical stiffness of a cantilever beam with the polynomial shape function assumption and  $\bar{N} = \frac{\pi^2 YI}{4L^2}$  is the critical axial load for a cantilever beam without tip mass and stiffness. Figure 5 shows the stable and unstable regions for different combinations of  $\hat{K}$  and  $\hat{N}$ . It should be noted that as  $\hat{K}$  approaches infinity  $\hat{N}_{cr}$  reaches the value of the critical axial load for a beam with clamped–pinned boundary conditions.

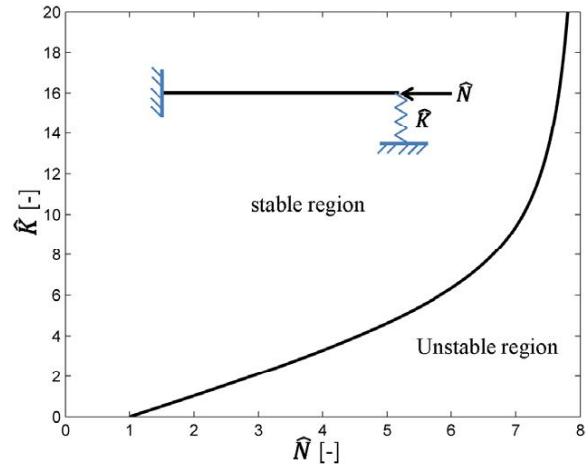


**Figure 5.** The normalized critical axial compressive load for different tip normalized stiffnesses of a cantilevered beam.

### 3.2. Electromechanical analysis of a bimorph with tip mass, stiffness and axial load

A detailed discussion of the coupled electrical circuit equations of a piezoelectric layer for series and parallel configurations under dynamic bending is beyond the scope of this paper. Readers may refer to [26, 29, 32] for more details. Considering the piezoelectric constitutive equations and Gauss' law, the steady state voltage response of the bimorphs shown in figure 4 for a series configuration is [26]

$$v_s(t) = \frac{\sum_{r=1}^{\infty} \frac{j\omega\kappa_r F_r}{\omega_r^2 - \omega + j2\xi_r\omega_r\omega}}{\frac{1}{R_l} + j\omega\frac{C_p}{2} + \sum_{r=1}^{\infty} \frac{j\omega\kappa_r \chi_r^s}{\omega_r^2 - \omega^2 + j2\xi_r\omega_r\omega}} e^{j\omega t} \quad (40)$$

and for a parallel configuration is

$$v_p(t) = \frac{\sum_{r=1}^{\infty} \frac{j\omega\kappa_r F_r}{\omega_r^2 - \omega + j2\xi_r\omega_r\omega}}{\frac{1}{2R_l} + j\omega C_p + \sum_{r=1}^{\infty} \frac{j\omega\kappa_r \chi_r^p}{\omega_r^2 - \omega^2 + j2\xi_r\omega_r\omega}} e^{j\omega t}. \quad (41)$$

In equations (40) and (41),  $F_r$  is the amplitude of the harmonic modal forcing function,  $\omega$  is the frequency of the base excitation,  $j$  is the unit imaginary number,  $\xi_r$  is the modal damping,  $\omega_r$  is the modal frequency,  $\kappa_r$  is the modal coupling term in the electric circuit,  $R_l$  is the resistive load in the electric circuit,  $C_p$  is the capacitance of each piezoelectric layer and  $\chi_r^s$  and  $\chi_r^p$  are modal electromechanical coupling terms.

For the base harmonic excitation given by equation (4), in which  $g(t) = Y_0 e^{j\omega t}$  and  $h(t) = \Psi_0 e^{j\omega t}$ , the modal harmonic forcing function is  $F_r e^{j\omega t}$ , where  $F_r$  is expressed as [26]

$$\begin{aligned} F_r = \omega^2 \left[ mY_0 \int_0^{L_c} \phi_r(x) dx + m\Psi_0 \int_0^{L_c} x\phi_r(x) dx \right. \\ \left. + M_t \phi_r(L)(Y_0 + L\Psi_0) \right] \end{aligned} \quad (42)$$

where  $Y_0$  and  $\Psi_0$  are the translational and small rotational displacement amplitudes of the base.

The modal electromechanical coupling terms  $\chi_r^s$  and  $\chi_r^p$  for series and parallel are

$$\chi_r^s = \left[ \Gamma \frac{d\phi_r(x)}{dx} \right]_{x=L_c} \quad \text{and} \quad \chi_r^p = \left[ 2\Gamma \frac{d\phi_r(x)}{dx} \right]_{x=L_c} \quad (43)$$

where  $\Gamma$  is defined in equation (13).

Also, the forward coupling term  $\kappa_r$  is expressed as

$$\kappa_r = e_{31}h_{pc}b \int_0^{L_c} \frac{d^2\phi_r(x)}{dx^2} dx = e_{31}h_{pc}b \left[ \frac{d\phi_r(x)}{dx} \right]_{x=L_c} \quad (44)$$

where  $h_{pc} = \frac{h_p+h_s}{2}$ . As was mentioned before, as far as modal analysis is concerned, the bimorph is identical in series and parallel connection configurations. However, the backward piezoelectric coupling effect that is manifested in the tip moment induced by the coupling term  $\kappa_r$  for an arbitrary electrical load is different for series and parallel connections of the piezoceramic layers, which affects the vibration response of the cantilever (the last term on the left hand side of equation (12)) [33].

Under the assumption that the electrode pairs covering the top and bottom faces of the piezoceramic layers are perfectly conductive, a single potential difference can be defined across the electrodes. The internal (inherent) capacitances of the piezoelectric layers are considered in the circuit along with a resistive electrical load (denoted by  $R_l$  in figure 4). The piezoceramic layers are assumed to be identical and their conductive electrodes are assumed to fully cover the respective surfaces (top and bottom) of these layers.

The capacitance  $C_p$  for each layer is

$$C_p = \frac{\varepsilon_{33}^S b L}{h_p} \quad (45)$$

where  $\varepsilon_{33}^S$  is the permittivity component at constant strain under the assumption of plane stress.

The normalized frequency response function (FRF) of the power output is

$$P(\omega) = \frac{|V|^2}{R_l g^2 \omega^2} \quad (46)$$

where  $g$  is the ground acceleration ( $9.81 \text{ m s}^{-2}$ ) and  $V$  is the amplitude of the steady state response in equations (40) and (41).

Although the power output of a piezoelectric harvester depends on the circuit design, in this paper only the mechanical effect on the electromechanical behavior of an optimal bimorph piezoelectric system is considered.

## 4. Numerical results

In this section a case study is presented to show the performance of the device based on the analytical model given in section 3. The geometric and material properties of the bimorph cantilever investigated are shown in tables 1 and 2 respectively.

**Table 1.** Geometric properties of the bimorph cantilever.

	Piezoceramic	Substructure
Length ( $L_c$ ) (mm)	100	100
Width <sup>a</sup> ( $b$ ) (mm)	15	15
Thickness ( $h_p, h_s$ ) (mm)	0.15	0.25

<sup>a</sup> The width for a dual beam is  $2 \text{ nm} \times 15 \text{ mm}$ . This is the value that is used in the model.

**Table 2.** Material properties of the bimorph cantilever.

	Piezoceramic	Substructure
Material	PZT-5A	Aluminum
Elastic modulus ( $c_{11}^E, Y_s$ ) (GPa)	61	70
Mass density ( $\rho_s, \rho_p$ ) ( $\text{kg m}^{-3}$ )	7750	2700
Piezoelectric constant ( $e_{31}$ ) ( $\text{C m}^{-2}$ )	-10.4	—
Permittivity constant ( $\varepsilon_{33}^S$ ) ( $\text{nF m}^{-1}$ )	13.3	—

**Table 3.** Modal frequency of the beam without tip mass, stiffness or axial load.

Mode	1	2	3	4	5
Frequency (Hz)	29.91	187.47	524.96	1028.7	1700.54
Modal damping ratio $\xi_r$	0.01	0.012	0.03	0.059	0.097

Figure 6 displays the normalized displacements and strain mode shapes for the first three vibration modes of the cantilevered beam without tip stiffness or axial load. The natural frequencies for the first five modes are given in table 3. The FRF of the power output for a series connection can be obtained by equations (40) and (46). Figure 7 shows the FRFs of power outputs, normalized to the square of the base acceleration (i.e.,  $g^2$ ), for different load resistances. To select the optimal load resistance, the maximum of the power output for each load resistance was calculated and the results are shown in figure 8. It can be observed that there are two optimal power operating points. One of these maxima is related to the mechanical resonance whereas the other one is related to the unit resonance as a result of the piezoelectric circuit contributions to the overall stiffness and mechanical behavior of the device [34]. To investigate the behavior of the proposed device the second optimal point (i.e.,  $368.9 \mu\text{W g}^{-2}$ ,  $109 \text{ k}\Omega$ ) is used throughout this paper.

### 4.1. Parametric study

Figure 9 shows the effects of the two parameters  $\hat{K}$  and  $\hat{N}$ , defined in section 3, on the natural frequency dimensionless parameter  $\hat{f}_n$  that is defined as the ratio between the frequency of the  $n$ th mode and the natural frequency of the first vibration mode without tip stiffness or axial load. Figure 9(a) shows the variation of the dimensionless natural frequencies of the first two vibration modes of the bimorph with tip stiffness ( $\hat{K}$ ), in the absence of axial load ( $\hat{N}$ ). As is expected, the natural frequencies of the first two modes increase as the stiffness

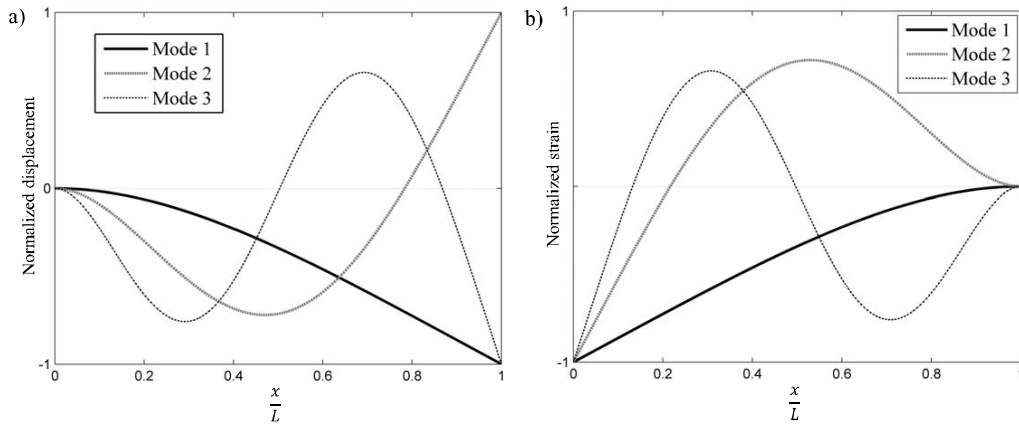


**Figure 6.** Normalized (a) displacement and (b) strain mode shapes of the cantilevered beam without tip stiffness or axial load for the first vibration modes.

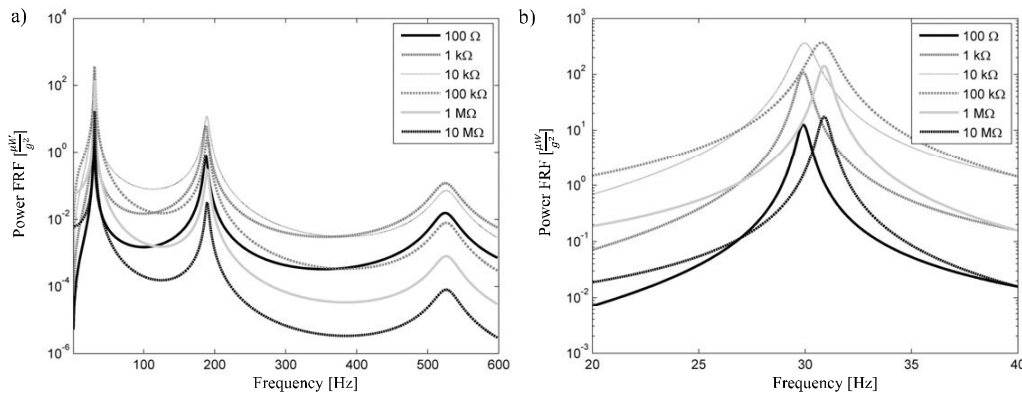


**Figure 7.** The power frequency response function of the bimorph without tip stiffness or axial load for series connection of the piezoceramic layers with (a) focus on the first three vibration modes and (b) focus on the first vibration mode.

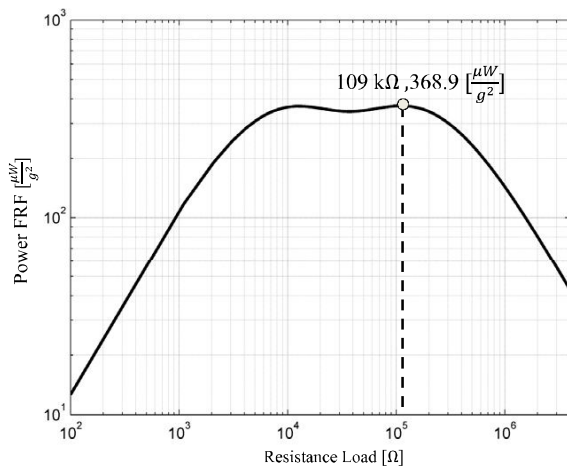


**Figure 8.** Variation of the maximum of power output with load resistance for all excitation frequencies and considering the five modes of vibration for the cantilevered beam without tip stiffness or axial load and considering a series configuration for the electric circuit.

of the dynamic system increases. It is noteworthy that the boundary conditions of the cantilevered harvester beam with a tip stiffness shift from clamped-free to clamped-pinned

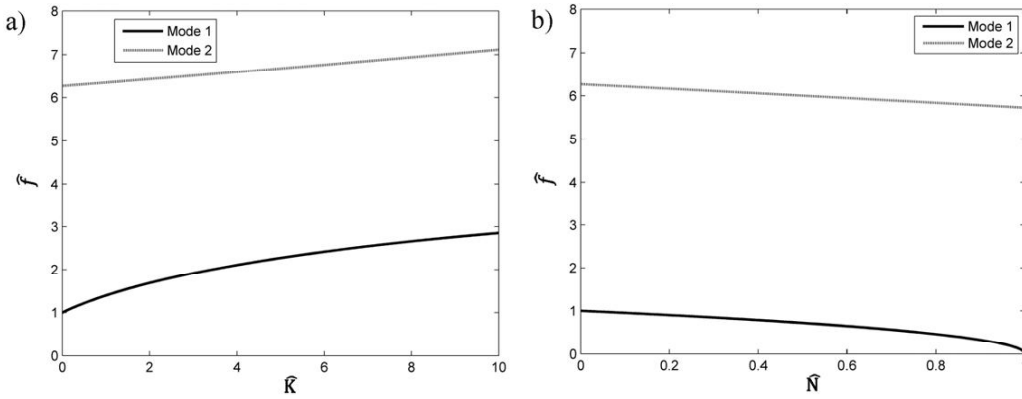
as  $\hat{K} \rightarrow \infty$ . In contrast, from figure 9(b) it can be inferred that, in absence of tip stiffness, by increasing the axial load the frequencies of the first two modes decrease. The reason behind this behavior is that an axial load provides a negative geometric stiffness, making the system softer. These two opposite effects can be combined by the proposed mechanism to control the dynamic response of the bimorph.

Figure 10 shows the variation of the first dimensionless modal frequency parameter versus the dimensionless tip stiffness and axial load. It should be mentioned that the frequency range covered by the device can be modified by changing the device parameters, such as the spring stiffness  $K_s$ .

The figure shows that the resonance frequency can be tuned to a wide range of frequencies using a combination of tip axial load and stiffness. Although the ability to tune the harvester with tip stiffness and axial load to very low (close to zero in the border of the stable region) and very large frequencies (in the limit of the resonance frequency of the clamped-pinned beam) is proved, the performance of the harvester in power generation should be appropriate in comparison with the power generation of a harvester without tip stiffness or axial load.

For evaluation of the efficiency of the bimorph with different tip stiffness and axial load combinations ( $\hat{P} =$





**Figure 9.** Variation of the dimensionless frequency parameter  $\hat{f}_n$  of the first and second vibration modes: (a) ratio of tip stiffness (no axial load), (b) ratio of tip axial load (no tip stiffness).

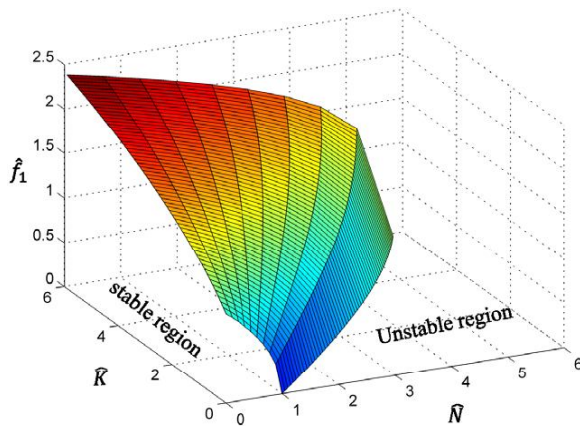


**Figure 10.** Variation of the dimensionless frequency parameter  $\hat{f}_n$  of the first vibration mode for combination of tip stiffness and axial load.

1 when  $\hat{K} = 0$  and  $\hat{N} = 0$ ), the dimensionless power generation parameter,  $\hat{P} = \frac{P_{\max} \text{ (with tip stiffness and axial load)}}{P_{\max} \text{ (without tip stiffness and axial load)}}$ , is shown in figure 11.

It can be seen that, in the absence of tip axial load, the power generation decreases by increasing the tip stiffness; this is caused by the increasing stiffness of the system and reduction in the displacement field of the harvester (reduction in the strain field as well). However, as can be observed in figure 11, the application of the axial load compensates the reduction of power generation even if the tip stiffness is increased. The physics behind this behavior is that the reduction in the general stiffness of the dynamic system as a result of the additional axial load leads to an increase of the displacement field of the harvester (the strain field increases). Hence, by applying the combination of tip stiffness and axial load, which is the main advantage of the proposed device, one can change the first modal frequency of the bimorph (figure 10) without significant effect on the power generation (figure 11). The specific design parameters of this device to tune to different frequencies and the corresponding numerical analysis are discussed in section 4.2.

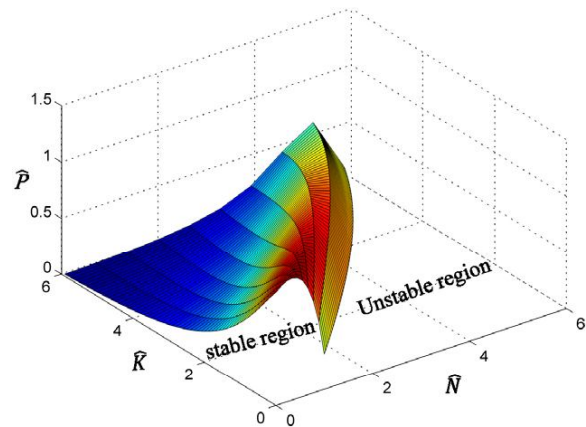


**Figure 11.** Variation of the dimensionless power generation parameter with respect to the dimensionless tip stiffness and axial load.

**Table 4.** The design properties of the device for the case study.

(Note that  $\alpha_0 = \tan^{-1} \frac{e \tan(\theta_0)}{a_0}$  and  $L_1 = \sqrt{(e \tan(\theta_0))^2 + a_0^2}$ .)

$\frac{K_s}{K}$	$\frac{N_{s0}}{N}$	$\theta_0$	$\theta_{\max}$	$e$ (cm)	$a_0$ (cm)
19.74	1.051	9.5°	25.5°	5	2.5

#### 4.2. A design specification for passive tuning of the device to different frequencies

Table 4 summarizes the design properties including the spring stiffness  $K_s$ , spring initial preload  $N_{s0}$ , initial spring angle  $\theta_0$ , maximum spring angle  $\theta_{\max}$  and  $e$  and  $a_0$  shown in figure 2. These design specifications are used to investigate the performance of the device. However, it should be pointed out that these parameters must be designed to obtain the frequency range of interest.

Figure 12 shows the relationship between  $d$  and  $\theta$ , obtained from equations (1) and (2), for three different values of  $a_0$ . Two main observations can be made: (1) the sensitivity of the angle  $\theta$  to  $d$  can be modified by changing  $a_0$  and (2)

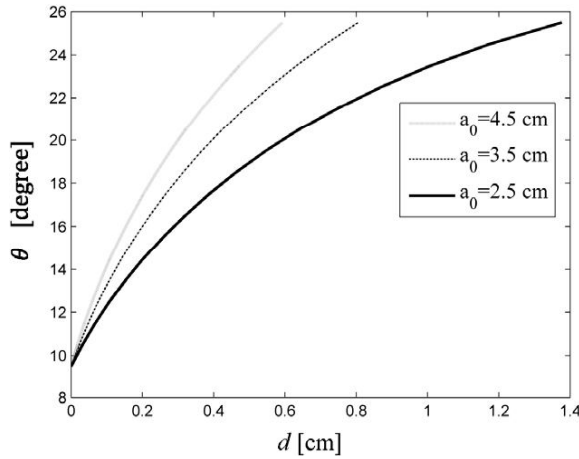


**Figure 12.** Variation of the angle  $\theta$  versus the displacement  $d$  for different  $a_0$ .

small displacements ( $d$ ) (e.g., between 0 and 1.4 cm) can be used to cover a range of angle  $\theta$  between  $9.5^\circ$  and  $25.5^\circ$ .

Figure 13 shows the power output FRF calculated in the range of angles covered using the design parameters in table 4. While the bimorph without tip mass or stiffness is just tuned to 29.1 Hz, this mechanism allows an operator to manually tune the device in a range of frequencies between 6 and 61.87 Hz, just by changing  $d$  between 0 and 1.4 cm.

Another interesting observation is that an initial increase of the maximum power output is followed by a decreasing trend. This behavior is caused by the strain distribution throughout the length of the beam, which affects the integrand in equation (44). Variations in the tip stiffness and axial load affect the natural frequencies and mode shapes; as a result, the modal strain along the length of the beam changes. Figure 14 shows the normalized first displacement and strain modal shape for different values of the angle  $\theta$ . In the first stage, increasing the angle changes the modal strain in a way that increases the integrand (increasing trend in figure 13). After the power FRF has reached a certain value (or certain

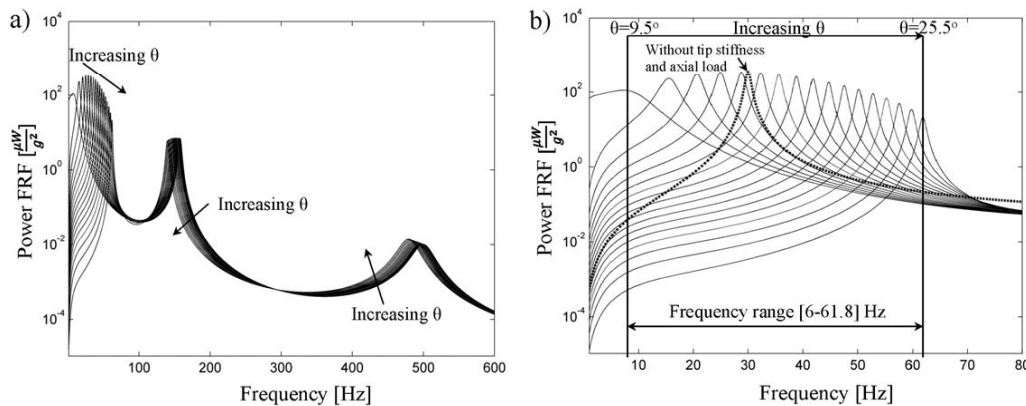
angle of the changing mechanism) this integrand decreases because of cancelation of the electrical output. A sign change for a vibration strain mode for a bimorph with a continuous electrode results in cancelation of the electrical output [33]. The change in strain sign for the first vibration mode is apparent in figure 14(b). Figure 15 shows that the effect of tip stiffness and axial load on the second strain mode is not as pronounced as on the first mode in this particular design.

To evaluate the stability of the device, figure 16 shows the variation of the normalized equivalent tip stiffness and axial load in the range of angle  $\theta$  obtained using the design parameters in table 4. The compressive critical axial load for this case study without tip stiffness is  $\bar{N} = \frac{\pi^2 YI}{4L^2} = 6.3471$  N. The approximate stiffness of the cantilevered beam without axial load or tip stiffness, assuming a polynomial mode shape, is  $\bar{K} = \frac{3YI}{L^3} = 77.17$  N m $^{-1}$ . It can be seen that change of the angle  $\theta$  within the range covered by the assumed design proprieties (e.g.,  $9.5^\circ$ – $25.5^\circ$ ) does not affect the stability of the device (i.e., the corresponding values of the equivalent tip stiffness and axial load stay within the stable region). It should be noted that one can use different design specifications listed in table 4 to change the combination of tip axial load and stiffness at changing mechanism  $d$  or angle  $\theta$  and thus match the desired design requirements path (the path is the inclined line shown in figure 16 for from  $\theta = 9.5^\circ$  or  $d = 0$  to  $\theta = 25.5^\circ$  or  $d = 1.4$  cm for the design specifications listed in table 4).

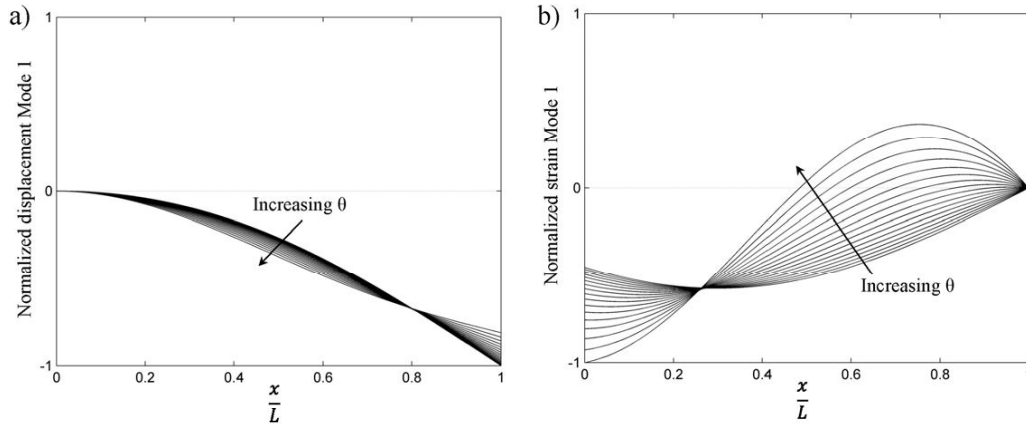
The dimensionless power generation  $\hat{P}$  of the system at different frequencies (different mechanism displacement  $d$  or angle  $\theta$ ) is shown in figure 17. As was discussed, although generally the power generation tends to decrease by increasing the tip stiffness, the tip axial load can compensate this effect reasonably.

Figure 18 shows the dimensionless fundamental modal frequency of the device corresponding to different angles. This device with the stated design specifications can cover a frequency range between 0 and almost two times the bimorph resonance frequency without tip stiffness and axial load.

Indeed, the line location, inclination and length (from  $\theta = 9.5^\circ$  to  $25.5^\circ$ ) shown in figures 16–18 can be changed



**Figure 13.** Power FRFs of the device for different values of the angle  $\theta$  of the design specifications for (a) the three first modes and (b) the first mode.



**Figure 14.** Variation of the normalized (a) displacement and (b) strain mode shapes for the first vibration mode with the angle for the proposed device.

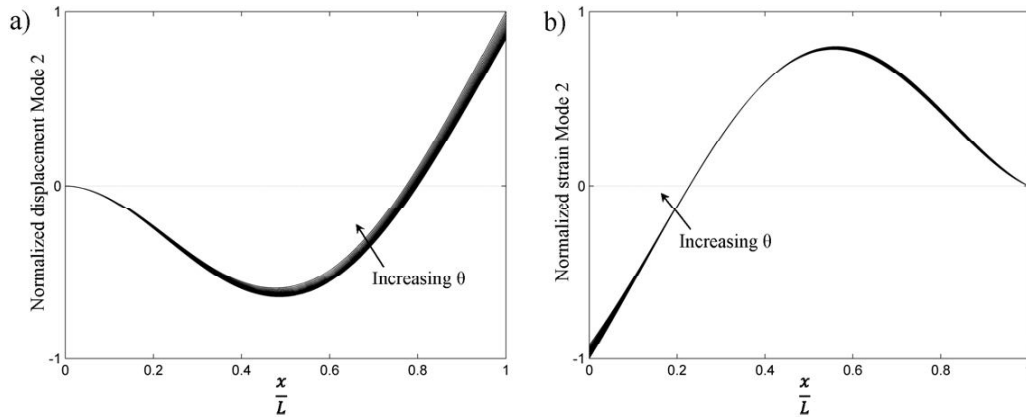


**Figure 15.** Variation of the normalized (a) displacement and (b) strain mode shapes of the second vibration mode with the angle for the proposed device.

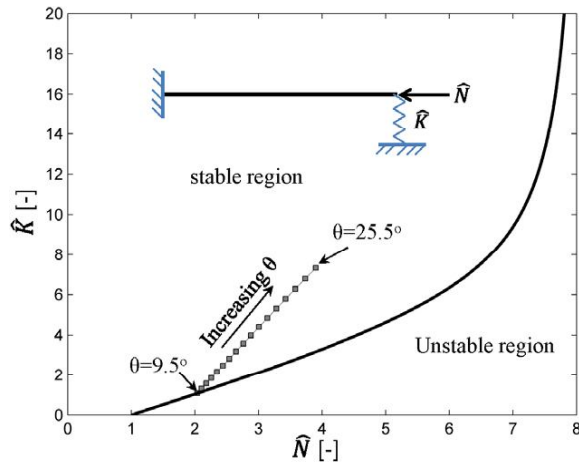


**Figure 16.** Equivalent tip stiffness and axial load at different angles  $\theta$  for the design specifications.

by selecting different design specifications like the spring stiffness  $K_s$ , spring initial preload  $N_{s0}$  and  $e$  to cover different ranges of frequencies with different paths.

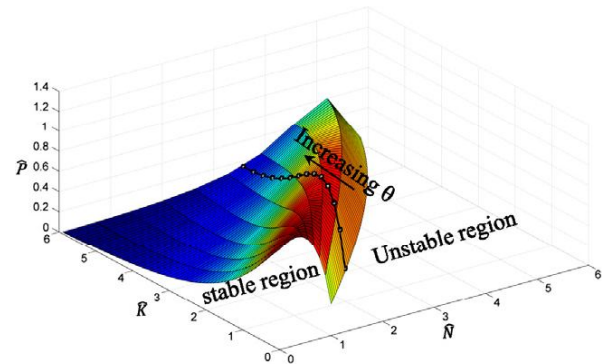


**Figure 17.** Variation of the dimensionless power generation parameter with respect to the dimensionless tip stiffness and axial load of the device with the design specifications shown in table 4.

To tune the frequency of the specified device to different frequencies one can adjust the displacement of the mechanism  $d$  according to figure 19. To provide the mechanism displacement  $d$ , it is suggested that the screw

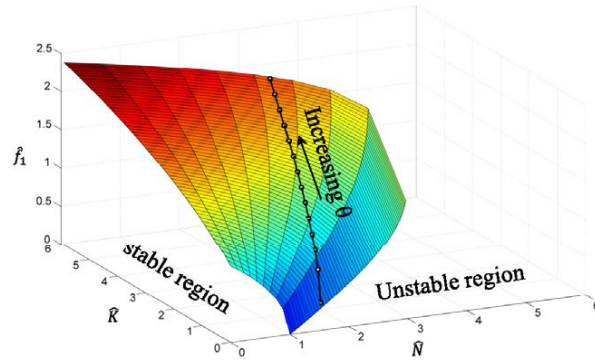


**Figure 18.** Variation of the dimensionless frequency parameter  $\hat{f}_1$  of the first vibration mode for a combination of tip stiffness and axial load of the device with the design specifications shown in table 4.

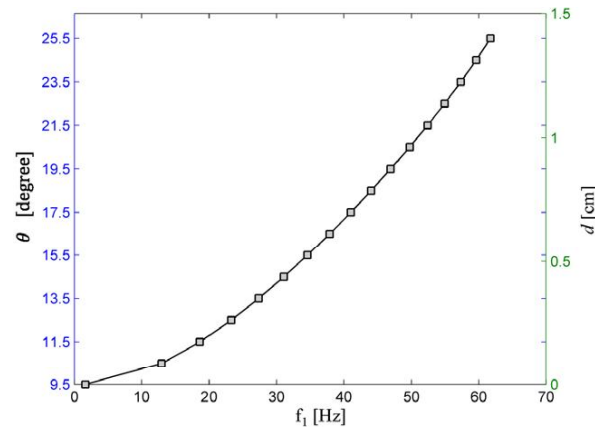


**Figure 19.** Variation of the tuning frequency with respect to the displacement of the mechanism  $d$  and the corresponding angle  $\theta$ .

connected to the simple joint at which the two levers meet each other should be used, figure 1 (this mechanical joint is horizontally and torsionally free). This screw can be found at the clamped connection at the end of the cantilevered energy harvester beam (figure 1). The pitch of this screw can be

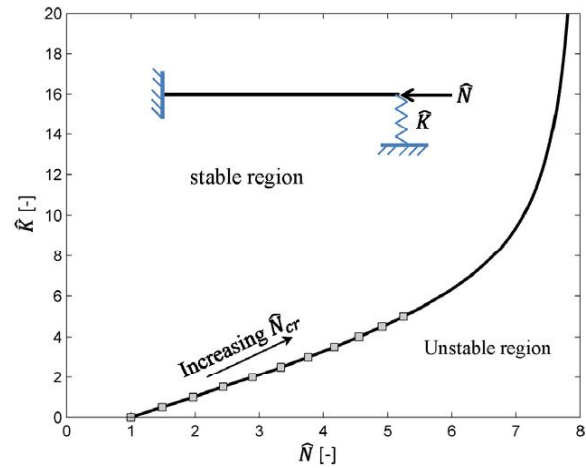


**Figure 21.** The equivalent tip stiffness and axial load in the proximity of the unstable region for a few selected  $\hat{N}_{cr}$  of the design specifications.

simply designed in such a way as to relate different screw revolutions to different frequencies.

To evaluate the sensitivity of the resonance frequency of the device to the displacement ( $d$ ) of the mechanism and spring angle  $\theta$  two sensitivity criteria are used,

$$S_d = \frac{df_1}{dd} \quad \text{and} \quad S_\theta = \frac{df_1}{d\theta}. \quad (47)$$

These two criteria are the derivatives of the fundamental frequency (i.e., frequency of the first modal vibration) with the displacement of the mechanism,  $d$ , and angle,  $\theta$ , respectively. Figure 20 shows variation of these two criteria with respect to the displacement of the mechanism,  $d$ , and angle,  $\theta$ . For these specific design parameters the sensitivity of the system decreases as  $d$  and  $\theta$  increase. At the beginning ( $d = 0$  or  $\theta = 9.5^\circ$ ), the fundamental vibration frequency of the bimorph can be changed by 35 Hz by just a one millimeter displacement of the mechanism; this value reduces to 1 Hz at  $d$  equal to 1.4 cm ( $\theta = 25.5^\circ$ ).

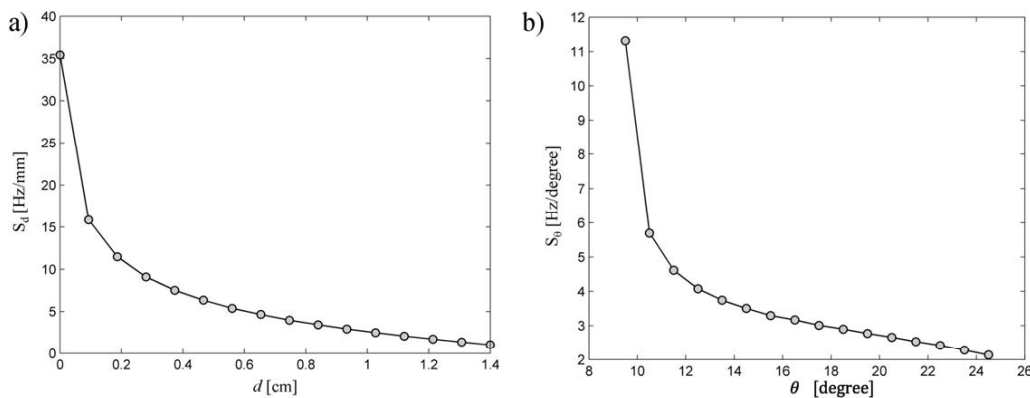


**Figure 20.** The sensitivity of the tuning frequency  $f_1$  to (a) the displacement  $d$  of the mechanism and (b) the angle  $\theta$ .

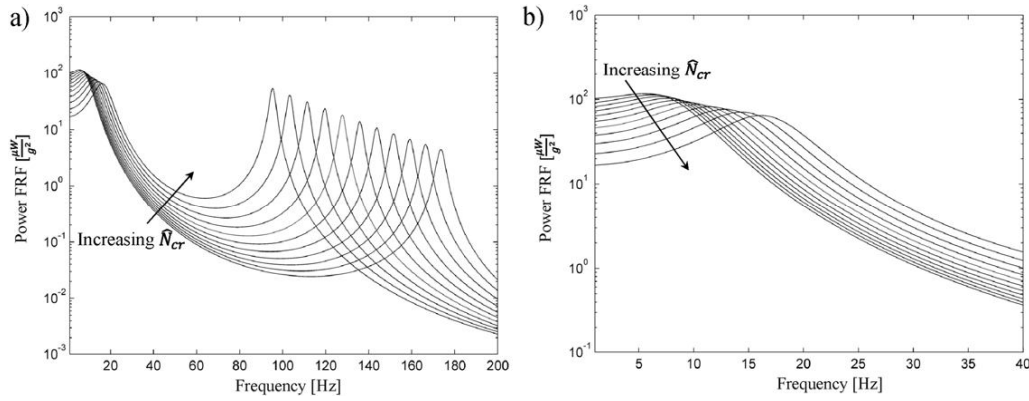


**Figure 22.** Power FRFs of the device for different  $\hat{N}_{cr}$  of the design specifications for (a) the two first modes and (b) the first mode.

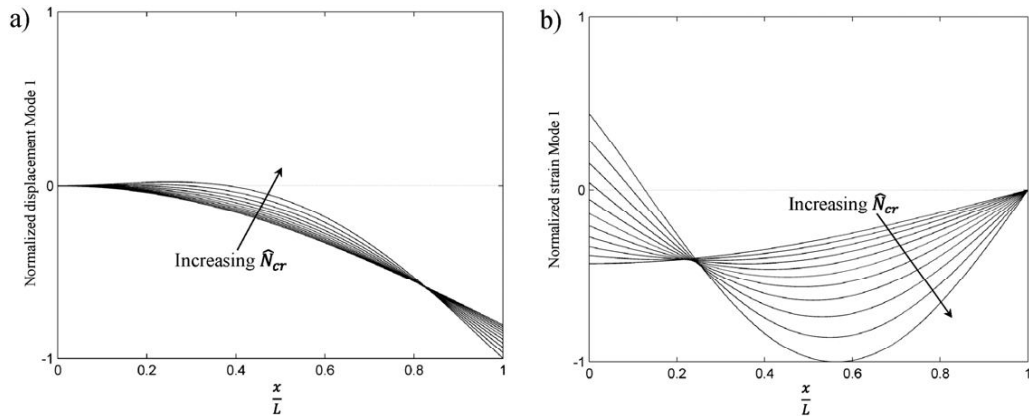


**Figure 23.** Variation of the normalized (a) displacement and (b) strain mode shapes of the first vibration mode for the proposed device with increasing  $\hat{N}_{cr}$ .

#### 4.3. Low frequency tuning

One of the main advantages of this device, apart from its capability to be passively tuned to different frequencies with small adjustments of the sliding mechanism, is that it can be theoretically tuned to frequencies close to zero, as can be observed in figure 13. In fact, the flat FRF achieved for an angle of  $\theta = 9.5^\circ$  (i.e., frequencies smaller than 6 Hz) shows that this device does not require a large proof mass to be tuned to low frequencies.

To show the capability of the device to provide flat and wideband power output FRFs for low frequencies, let us consider a set of normalized tip stiffnesses and axial loads in the borderline region, as shown in figure 21. Figure 22 shows the corresponding power output FRFs. As the boundary condition of the bimorph with the axial load on the stable border gets closer to the clamped–pinned boundary condition, the maximum power output decreases and the device FRF supports a wider band of frequencies. As a result, the device can be tuned to a wider range of low frequencies in the borderline region, without losing significant efficiency. Further, the maximum power output for the second mode increases by moving up along this region. Figure 23 shows the variation of the normalized first displacement and strain

modal shape for the corresponding points shown in figure 21. The integrand of the first strain mode decreases gradually and this is why the FRF of the power output decreases (the first peaks in figure 22). On the other hand, the power output of the second mode increases as a result of changing the second strain node, which results in less cancelation of power. The normalized displacement and strain of the second mode are displayed in figure 24.

#### 5. Conclusion

A novel dual cantilevered piezoelectric energy harvester with variable tip stiffness and axial load was presented. A differential equation for an axially loaded cantilevered beam with tip stiffness, based on Euler–Bernoulli beam assumptions, was developed and the characteristic function for multimode vibration of the beam based on the boundary conditions was derived. The frequency response function of the power output was used to evaluate the performance of the system. The effects of dimensionless tip axial load and stiffness on the resonance frequency and power generation of the harvester have been discussed. Increase of the tip stiffness increases the resonance frequency; conversely, compressive



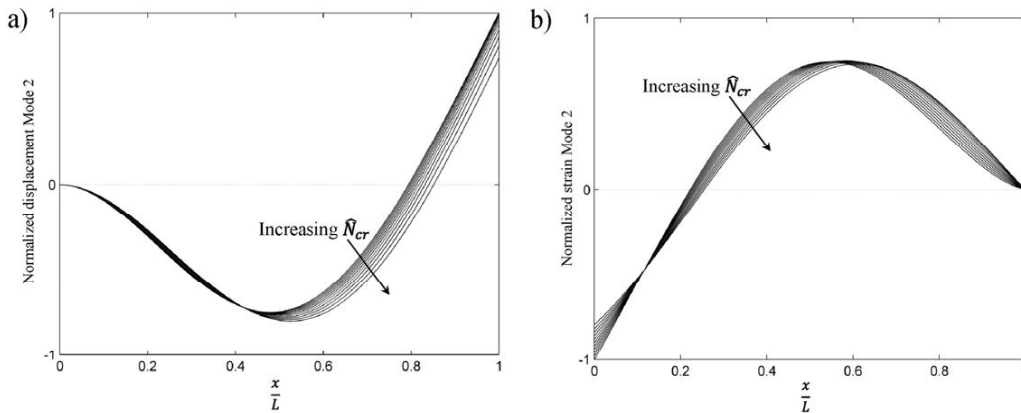


**Figure 24.** Variation of the normalized (a) displacement and (b) strain mode shapes of the second vibration mode for the proposed device with increasing  $\hat{N}_{cr}$ .

axial load decreases the resonance frequency of the harvester. It was shown that, although increase of the tip stiffness causes a reduction in power generation as a result of reduction of the displacement field, this can be compensated by application of an axial load that reduces the general stiffness of the dynamic system.

The behavior of the proposed device with design specifications in the stable region was numerically investigated and it was shown that it is able to passively tune to different frequencies by small adjustments of the proposed sliding mechanism. Furthermore, the results showed that this device can be used to tune the energy harvester to very low frequencies without the need of a large proof mass.

### Acknowledgments

The authors would like to thank Mehdi Maneshi for preparing figures 1 and 2. The authors would also like to thank Amir Rezaei-Bazkiaei for his help in running the numerical program at the Center for Computational Research (CCR) at the State University of New York at Buffalo. The first author would like to kindly express his appreciation to Mrs Saba Hosseini Rudsari for her positive encouragement.

### References

- [1] Roundy S, Wright P K and Rabaey J M 2004 *Energy Scavenging for Wireless Sensor Networks: With Special Focus on Vibrations* (Dordrecht: Kluwer)
- [2] Leland E S and Wright P K 2006 Resonance tuning of piezoelectric vibration energy scavenging generators using compressive axial preload *Smart Mater. Struct.* **15** 1413–20
- [3] Shahruz S 2006 Design of mechanical band-pass filters for energy scavenging *J. Sound Vib.* **292** 987–98
- [4] Challa V R, Prasad M G, Shi Y and Fisher F T 2008 A vibration energy harvesting device with bidirectional resonance frequency tunability *Smart Mater. Struct.* **17** 015035
- [5] Roundy S *et al* 2005 Improving power output for vibration-based energy scavengers *IEEE Pervasive Comput.* **4** 28–36
- [6] Sterken T, Baert K, Van Hoof C, Puers R, Borghs G and Fiorini P 2004 Comparative modeling for vibration scavengers [MEMS] energy scavengers *Proc. IEEE Sensors* pp 1249–52
- [7] Roundy S 2005 On the effectiveness of vibration-based energy harvesting *J. Intell. Mater. Syst. Struct.* **16** 809–23
- [8] Shen D, Park J H, Ajitsaria J, Choe S Y, Wickle H C and Kim D J 2008 The design, fabrication and evaluation of a MEMS PZT cantilever with an integrated Si proof mass for vibration energy harvesting *J. Micromech. Microeng.* **18** 055017
- [9] Sebald G, Kuwano H, Guyomar D and Ducharme B 2011 Simulation of a Duffing oscillator for broadband piezoelectric energy harvesting *Smart Mater. Struct.* **20** 075022
- [10] Hajati A and Kim S G 2011 Ultra-wide bandwidth piezoelectric energy harvesting *Appl. Phys. Lett.* **99** 083105
- [11] Soliman M S M, Abdel-Rahman E M, El-Saadany E F and Mansour R R 2008 A wideband vibration-based energy harvester *J. Micromech. Microeng.* **18** 115021
- [12] Liu H, Lee C, Kobayashi T, Tay C J and Quan C 2012 Investigation of a MEMS piezoelectric energy harvester system with a frequency-widened-bandwidth mechanism introduced by mechanical stoppers *Smart Mater. Struct.* **21** 035005
- [13] Liu H, Tay C J, Quan C, Kobayashi T and Lee C 2011 Piezoelectric MEMS energy harvester for low-frequency vibrations with wideband operation range and steadily increased output power *J. Microelectromech. Syst.* **20** 1131–42
- [14] Cornwell P J 2005 Enhancing power harvesting using a tuned auxiliary structure *J. Intell. Mater. Syst. Struct.* **16** 825–34
- [15] Roundy S 2005 Toward self-tuning adaptive vibration-based microgenerators *Proc. SPIE* **5649** 373–84
- [16] Anton S R and Sodano H A 2007 A review of power harvesting using piezoelectric materials (2003–2006) *Smart Mater. Struct.* **16** R1–R21
- [17] Wu X, Lin J, Kato S, Zhang K, Ren T and Liu L 2008 A frequency adjustable vibration energy harvester *Proc. PowerMEMS*
- [18] Jo S E, Kim M S and Kim Y J 2011 Passive-self-tunable vibrational energy harvester *Solid-State Sensors, Actuators and Microsystems Conf. (TRANSDUCERS)* pp 691–4
- [19] Gu L and Livermore C 2010 Passive self-tuning energy harvester for extracting energy from rotational motion *Appl. Phys. Lett.* **97** 081904
- [20] Gu L and Livermore C 2012 Compact self-tuning passively energy harvesting for rotating applications *Smart Mater. Struct.* **21** 015002
- [21] Lesieutre G A and Davis C L 1997 Can a coupling coefficient of a piezoelectric device be higher than those of its active material? *J. Intell. Mater. Syst. Struct.* **8** 859–67

- [22] Hu Y, Xue H and Hu H 2007 A piezoelectric power harvester with adjustable frequency through axial preloads *Smart Mater. Struct.* **16** 1961–6
- [23] Eichhorn C, Goldschmidtboeing F and Woias P 2009 Bidirectional frequency tuning of a piezoelectric energy converter based on a cantilever beam *J. Micromech. Microeng.* **19** 094006
- [24] Karami M A and Inman D J 2012 Parametric study of zigzag microstructure for vibrational energy harvesting *IEEE J. Microelectromech. Syst.* **21** 145–60
- [25] Leet K M, Uang C M and Gilbert A M 2005 *Fundamentals of Structural Analysis* (New York: McGraw-Hill)
- [26] Erturk A and Inman D J 2011 *Piezoelectric Energy Harvesting* (New York: Wiley)
- [27] Virgin L N 2007 *Vibration of Axially Loaded Structures* (Cambridge: Cambridge University Press)
- [28] Auld B A 1973 *Acoustic Fields and Waves in Solids* (New York: Wiley)
- [29] Erturk A and Inman D J 2009 An experimentally validated bimorph cantilever model for piezoelectric energy harvesting from base excitations *Smart Mater. Struct.* **18** 025009
- [30] Clough R W and Penzien J 1975 *Dynamics of Structures* (New York: McGraw-Hill)
- [31] Leipholz H 1970 *Stability Theory: An Introduction to the Stability of Dynamic Systems and Rigid Bodies* (New York: Academic)
- [32] Erturk A and Inman D J 2008 A distributed parameter electromechanical model for cantilevered piezoelectric energy harvesters *J. Vib. Acoust.* **130** 041002
- [33] Erturk A, Tarazaga P A, Farmer J R and Inman D J 2009 Effect of strain nodes and electrode configuration on piezoelectric energy harvesting from cantilevered beams *J. Vib. Acoust.* **131** 011010
- [34] Dutoit N E, Brian L W and Sang-Gook K 2005 Design considerations for MEMS-scale piezoelectric mechanical vibration energy harvesters *Integr. Ferroelectr.* **71** 121–60